# Tracing multiple scattering patterns in absolute ($e,2e$) cross sections for $H_2$ and He over a $4\pi$ solid angle

X. Ren,[1] A. Senftleben,[1] T. Pflüger,[1] A. Dorn,[1] J. Colgan,[2] M. S. Pindzola,[3] O. Al-Hagan,[4] D. H. Madison,[4] I. Bray,[5] D. V. Fursa,[5] and J. Ullrich[1]

[1]*Max-Planck-Institute for Nuclear Physics, 69117 Heidelberg, Germany*
[2]*Theoretical Division, Los Alamos National Laboratory, Los Alamos, New Mexico 87545, USA*
[3]*Department of Physics, Auburn University, Auburn, Alabama 36849, USA*
[4]*Physics Department, Missouri University of Science and Technology, Rolla, Missouri 65409, USA*
[5]*ARC Centre for Antimatter-Matter Studies, Curtin University, G.P.O. Box U1987 Perth, Western Australia, Australia*
(Received 12 July 2010; published 27 September 2010)

Absolutely normalized ($e,2e$) measurements for $H_2$ and He covering the full solid angle of one ejected electron are presented for 16 eV sum energy of both final state continuum electrons. For both targets rich cross-section structures in addition to the binary and recoil lobes are identified and studied as a function of the fixed electron's emission angle and the energy sharing among both electrons. For $H_2$ their behavior is consistent with multiple scattering of the projectile as discussed before [Al-Hagan *et al.*, Nature Phys. **5**, 59 (2009)]. For He the binary and recoil lobes are significantly larger than for $H_2$ and partly cover the multiple scattering structures. To highlight these patterns we propose a alternative representation of the triply differential cross section. Nonperturbative calculations are in good agreement with the He results and show discrepancies for $H_2$ in the recoil peak region. For $H_2$ a perturbative approach reasonably reproduces the cross-section shape but deviates in absolute magnitude.

PACS number(s): 34.80.Dp

## I. INTRODUCTION

A large part of our knowledge of the dynamical behavior of quantum mechanical few-body systems is based on charged particle impact ionization studies of fundamental atomic systems. In particular, kinematically complete studies for electron-impact ionization have a long and very successful history. They determine the momentum vectors of both final state continuum electrons, thereby allowing for stringent tests of theoretical models. Recent years have shown fast progress of nonperturbative calculations, obtaining essentially exact solutions of the fundamental three-body problem of ($e,2e$) for the one-electron target atomic hydrogen [1–3]. Furthermore, they proved to be very accurate in most cases for single ionization of helium [4]. These theories presently are developed toward more complex, e.g., four-body, systems such as the lithium atom and the hydrogen molecule [5,6]. Perturbative models have improved significantly as well, although they do not claim to be exact due to the underlying approximations. Compared to nonperturbative models, more complex target systems can be treated fairly accurately, including heavy atoms [7] and molecules [8]. One of the important advantages of a perturbation approach lies in the fact that intuitive insight into the reaction dynamics can be obtained by switching on and off specific interactions in the model and observing the resulting changes in the cross sections. Consequently, important knowledge is obtained on the essential interactions and contributions in the collision.

Most ($e,2e$) experiments have been performed in coplanar geometry where both final state electrons move in a plane containing the incoming beam. In this scattering plane the highest cross sections are observed due to first-order projectile-target interactions resulting in the well-known binary and recoil lobes. In recent years, experiments outside the coplanar geometry have identified higher-order or multiple scattering

processes [9–13]. The systematic investigation of these non-coplanar geometries was initiated by Murray *et al.* [9,14] for electron projectiles using a conventional ($e,2e$) apparatus. Using the reaction microscope technique, Schulz *et al.* [11] obtained the first three-dimensional (3D) cross section images for ion-impact ionization and identified significant intensity perpendicular to the scattering plane. In this work and in subsequent experimental and theoretical studies the out-of-plane intensity was attributed to projectile scattering in the Coulomb potential of the nucleus additionally to the binary collision with the target electron [15]. Subsequently, similar observations were made in ($e,2e$) studies for helium at high and medium impact energy and for heavier target species such as magnesium or argon [7,16]. It turned out that some theoretical models that obtained good agreement in the coplanar scattering plane fail in reproducing these so-called out-of-plane structures, and it was shown that it is essential to account for the proper atomic potential within the scattering model.

Motivated by these observations, ($e,2e$) studies have re-considered molecular targets where, compared to atoms, the multiple-center target structure should lead to significantly different cross sections. This is the case at high impact energy where the electron's de Broglie wavelength is comparable to or shorter than the internuclear distance, so that interference phenomena are expected [17–19], and at low impact energy in phase space regions where nuclear scattering is dominant. For example, Al-Hagan *et al.* [20] have obtained detailed information on multiple collisions and electron-electron correlation in the ionization process by analyzing the cross section for the situation where both final state electrons are emitted perpendicular to the incoming beam (henceforth referred to as the perpendicular plane). This was possible by performing perturbative quantum mechanical calculations of different degrees of sophistication. Additionally, results for two targets

with equal numbers of electrons, molecular $H_2$ and atomic He, were directly compared. The triply differential cross section (3DCS) was obtained for final state electrons having 10 eV energy as a function of the relative angle between the outgoing electrons. The measurements revealed for both targets peaks around $120°$ relative angle, which were assigned to elastic scattering of the projectile from the target into the perpendicular plane and a subsequent binary collision with the target electron. For helium an additional dominating maximum at $180°$ was concluded to be due to the same collision sequence with subsequent backscattering of one final state electron. This results from the much stronger gradient of the He potential well produced by the concentration of positive charge at the center of mass. Subsequent studies have been performed for unequal energy sharing and particular electron emission planes in between the perpendicular and the coplanar scattering plane [21]. The nonabsolute measurements revealed surprising discrepancies with the nonperturbative time-dependent close-coupling theory (TDCC) that so far have not been explained. Finally, results for the perpendicular plane showing increasing back-to-back emission for decreasing energies of the electrons were discussed in terms of final state repulsion between both electrons in the vicinity of the threshold [22].

While the mentioned studies for the $H_2$ and He targets showed a fairly consistent picture of the perpendicular plane cross section being due to multiple scattering, new experimental results for various noble gases revealed complex variations of the emission pattern in the perpendicular plane as a function of the incident energy and target [23]. At a first glance these new results do not easily fit into the picture drawn above and therefore further theoretical and experimental studies are required. For example, all $H_2$ experiments cited above were performed for randomly aligned molecules even though the multiple scattering dynamics should sensitively depend on the alignment of the molecular axis with respect to the incoming beam, as was demonstrated by TDCC calculations [6]. At high [24] and intermediate [25,26] impact energy, the feasibility of performing (*e*,2*e*) experiments on $H_2$ with known molecular axis has been demonstrated. This has not yet been achieved in the low-energy regime and for the perpendicular plane where the cross section is comparatively small.

Here we report on an (*e*,2*e*) study for the helium and molecular hydrogen targets at similar impact energy as chosen by Al-Hagan *et al.,* with the outgoing electron's sum energy of 16 eV. With the present work we accomplish several objectives: On one hand, this study provides 3D cross sections in the low-energy range covering the full solid angle of electron emission and is not restricted to particular emission planes. As a result we are in a situation to recognize that the previously mentioned cross-section maxima for $H_2$ and He in the perpendicular plane originate from a richly structured 3D pattern. Its shape sensitively depends on the details of the scattering kinematics. The variation of the cross section as a function of energy sharing allows further insight into the underlying multiple scattering effects. Second, we provide absolutely normalized cross sections in order to judge theories not only concerning the shape but also the magnitude of the cross section. In particular, in the light of the above-mentioned discrepancies between state-of-the-art nonperturbative calculations

and existing relative experiments, this is highly desirable. Finally, we discuss an alternative representation of the 3DCS that highlights the presence of identical cross-section patterns due to multiple collisions for both targets hydrogen and helium.

## II. EXPERIMENTAL SETUP

The measurements were performed using a reaction microscope [27] which is specially designed for electron collision experiments. The setup has been described before [13,28], and only a brief description will be given here. A well focused (1 mm diameter), pulsed electron beam (pulse width 1.5 ns), produced by a standard thermocathode gun, intersects a cold $H_2$ or He gas jet (2 mm diameter) created by supersonic expansion. Using parallel electric and magnetic fields, the final state electrons and the recoiling ion are projected onto two-dimensional position- and time-sensitive detectors in opposite directions. From the positions of the hits and the times of flight, the initial momentum vectors of the detected fragments can be determined. A large part of the full $4\pi$ solid angle is covered for final state particles, 100% for the detection of the recoil ion and about 80% for electrons. These miss the detector for energies higher than 12 eV energy and for particular times of flight where they arrive close to the spectrometer axis in a bore on the electron detector. In the present measurement only one of the outgoing electrons (momentum $\vec{k}_1$) and the recoil ion ($\vec{k}_r$) are measured in coincidence. The other electron momentum ($\vec{k}_2$) is then calculated using momentum conservation. This method is advantageous since, for fixed energy and emission angle of the detected electron, the large acceptance for the recoil ion can be exploited to reconstruct the second electron's momentum over the full solid angle and for energies exceeding the electron spectrometer acceptance. The drawback is the rather limited ion momentum resolution of about 0.2 a.u. in the transverse direction (with respect to the incoming electron beam) and 0.1 a.u. in longitudinal direction compared to 0.05 a.u. for the electron spectrometer. As a result the angular resolution for a reconstructed electron with kinetic energy of 8 eV is $6°$ (full width at half maximum FWHM) if emitted in the transverse direction and $12°$ if emitted in the forward or backward direction.

For the kinematics of our present experiments, the excess energy is fixed to 16 eV for both $H_2$ and He ionization. The incident energy ($E_0$) is appropriately adjusted to fulfill the energy conservation requirement for the different targets, $E_0 = E_1 + E_2 + V_i$, where $V_i$ is the ionization potential (24.6 eV for He and 15.5 eV for $H_2$). Thus, the beam energies are $E_0 = 40.6$ eV for He and $E_0 = 31.5$ eV for $H_2$. The projectile beam is aligned along the $z$ axis of the coordinate system utilized as indicated by $\vec{k}_0$ in Fig. 1(a).

As mentioned above, the experimental data are obtained on an absolute scale. For He, our measured 3DCSs are directly compared with the previous absolute measurements for $E_0 = 40$ eV in coplanar geometry by Röder *et al.* [29]. Excellent agreement between these two data sets was achieved concerning their shape [30]. The uncertainty of the absolute scale was estimated to be less than 22% according to [29,31]. For $H_2$, our experimental 3DCS for a particular polar angle of one electron ($\theta_1 = -90°$) and energy sharing $E_1 = 4$ eV, $E_2 = 12$ eV is integrated over the whole $4\pi$ solid angle
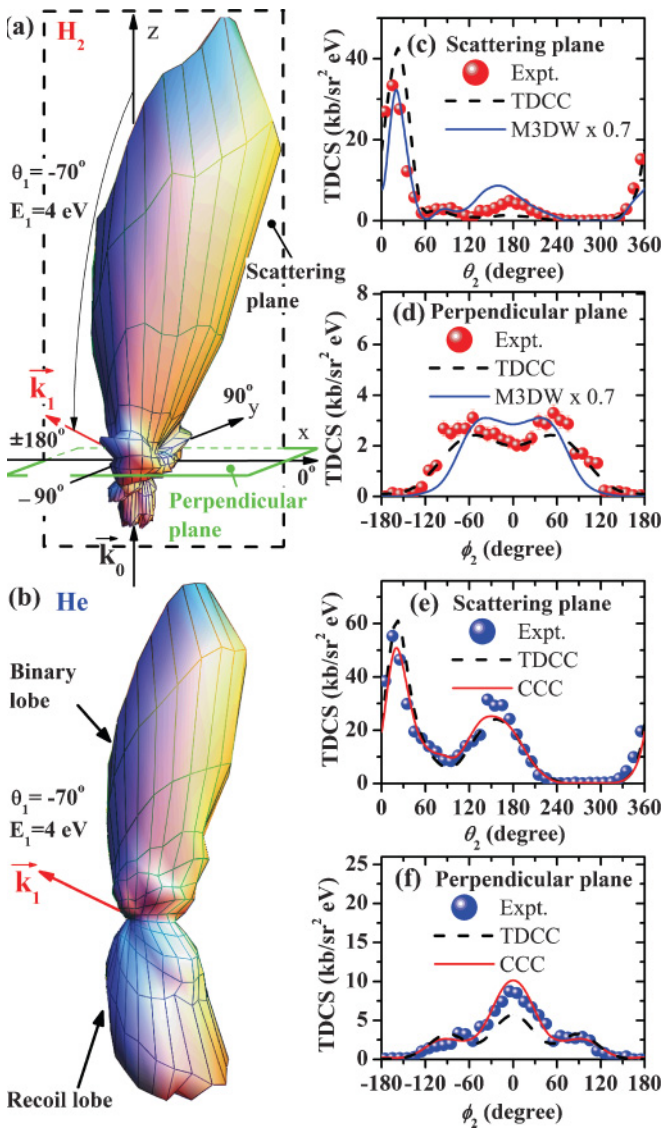
FIG. 1. (Color online) 3DCS for $H_2$ (three top diagrams) and He (three bottom diagrams) as a function of the emission angle of an electron with kinetic energy $E_2 = 12$ eV. The emission angle of the other electron ($E_1 = 4$ eV) is fixed to $\theta_1 = -70°$: (a) and (b) Experimental 3D-cross sections for $H_2$ and He, respectively: (c) and (d) Cross section cuts for $H_2$ in the scattering and perpendicular planes, respectively. $\phi_2$ is the emission angle in the perpendicular plane with respect to the $x$-axis. The experimental data are given by full circles. (e) and (f) same as (c) and (d) but for He.

for emission of the second electron. It is then normalized to the published absolute double differential cross sections (DD-CSs) [32,33]. As result the absolute scale for all experimental data of $H_2$ is fixed. The uncertainty of the absolute scale is determined by the accuracy of the measured DDCSs, which was stated to be $\pm16\%$ [32].

## III. THEORY

We compare the $H_2$ measurements with calculated cross sections from the time-dependent close-coupling (TDCC) theory and the three-body distorted wave (M3DW) model.

The helium data are compared to TDCC and convergent close-coupling (CCC) calculations.

The TDCC method [34] as used for ionization of $H_2$ is briefly outlined in [35]. It is based on the expansion of the outgoing electron-pair wave function in position space. This leads to a set of time-dependent close-coupled partial differential equations which include the direct and local exchange potentials with the nonionized (frozen) electron. For an initial Gaussian wave packet the equations are propagated in time and finally projected onto suitable products of continuum wave functions of the ionic target. In the case of $H_2$ the 3DCSs are computed for all possible molecular angles and then averaged to compare with the measurements on nonaligned molecules. The TDCC approach was recently shown to produce good agreement in shape with 3DCSs in the perpendicular plane with equal electron energies of 10 eV each. On the other hand, strong and so far unexplained discrepancies with experiment were found in the relative 3DCS magnitude in a comparison of scattering plane and perpendicular plane results [35]. For He good agreement was found for various kinematics [36].

In the M3DW model [37,38] the $T$-matrix element is calculated using an initial bound state wave function that is the orientation-averaged molecular wave function for $H_2$. The incident, scattered, and ejected electrons are described by distorted waves. The incoming distorted wave is calculated using an orientation-averaged molecular potential consisting of a static potential containing the electronic and nuclear parts, an exchange potential accounting for exchange with the bound electrons, and a correlation-polarization potential. The distorted waves in the final state are calculated in the same manner except that the charge distribution of an ion is used. In addition a Coulomb-distortion factor in the $T$-matrix element accounts for the repulsion of the two final state continuum electrons.

Details of the CCC method have been given by Bray and Fursa [39] and Stelbovics et al. [40]. Briefly, the target states are obtained by diagonalizing the target Hamiltonian in a complete Laguerre basis, and the close-coupling equations are solved utilizing the momentum space representation. In the frozen-core treatment, one of the He electrons is described by the $1s$ orbital of $He^+$. The CCC method has been applied extensively and successfully to $e$-He single ionization at various energies [41,42].

## IV. RESULTS

Examples of three-dimensional cross sections of $H_2$ and He are presented in Figs. 1(a) and 1(b) as 3D polar plots. The projectile with momentum $k_0$ is coming in from below and scatters off the target at the origin of the coordinate system displayed in Fig. 1(a). The emission angle of a slow final state electron with $E_1 = 4$ eV is fixed to $\theta_1 = -70°$ with respect to the projectile forward direction, while the emission angle of a faster electron ($E_2 = 12$ eV) is varied over the full $4\pi$ solid angle. In these diagrams, the 3DCS for emission into a particular direction is given as the distance from the origin of the plot to the point on the 3D surface which is intersected by the electron's trajectory.

At high-energy electron impact, the cross-section patterns are governed by a binary peak (the forward lobe)

corresponding to the direct knockout of the target electron and its emission along the momentum transfer and a recoil lobe (the smaller backward lobe) originating from backscattering of the forward-emitted electron in the nuclear potential. Unlike fast collisions, in the present low-energy case ($H_2$, $k_0 \approx 1.5$ a.u.; He, $k_0 \approx 1.7$ a.u.) pure binary collisions are not favored. This is because the momenta of both final state electrons are rather small ($k_1 \approx 0.54$ a.u.; $k_2 \approx 0.94$ a.u.) and add up to $k_0$ only if both are emitted collinearly forward in the case of $H_2$, or they even cannot carry the projectile momentum at all in the case of He. Thus, a binary electron-electron collision, without active participation of the nucleus, can cause the observed forward lobe only if nonzero momentum components of the initial bound electron wave function in the momentum representation (the "Compton profile") are involved. Due to the higher binding energy of He compared to $H_2$, its Compton profile is significantly wider. Therefore, for the given kinematics He has a higher absolute cross section for the binary lobe. This can be seen in the right column of Fig. 1, where cuts through the 3D images of the absolutely normalized cross sections within the "scattering" plane [Figs. 1(c) and 1(e)] and the "perpendicular" plane with respect to the incoming beam [Figs. 1(d) and 1(f)] are shown. We find that the ratio of the respective binary peak heights for He and $H_2$ is about 1.6, which is in strong contrast to the total ionization cross sections at the present impact energy, for which $H_2$ is higher by a factor of 4 compared to He [43]. The additional scattering of the fast outgoing electron in the ionic potential gives rise to the recoil lobe directed along the backward direction. For $H_2$ the two positive nuclear charges are spatially separated, and the resulting shallow ionic potential leads to a relatively small recoil lobe. For He, on the other hand, the two positive charges are concentrated in one point and the resulting high potential gradient clearly leads to a significantly stronger recoil lobe. These dissimilar target potentials and the resulting implications for the projectile-nucleus scattering were also invoked to explain different amplitudes for higher-order scattering processes. As mentioned in the introduction, Al-Hagan *et al.* [20] studied the perpendicular geometry, observing two maxima corresponding to dominant $120°$ relative emission angle for $H_2$ and dominant back-to-back emission for He. In Figs. 1(d) and 1(f) we show comparable cuts of the 3D patterns within this perpendicular plane, which is indicated in Fig. 1(a). Despite the fact that the fixed electron here is emitted $20°$ out of the perpendicular plane ($\theta_1 = -70°$) for $H_2$, we still find two peaks in the 3DCS at $\phi_2 = \pm 60°$ with respect to the *x* axis. These correspond again to about a $120°$ relative angle between the two final state electrons. For He a strong $\phi_2 = 0°$ peak, i.e., dominant back-to-back emission, is present.

From the 3D plots a more general view is obtained, revealing for $H_2$ a *U*-shaped ridge culminating in two slightly forward-tilted lobes filling the 3DCS minimum between the binary and recoil lobes. From its structure it becomes clear that there are no singular cutting planes which can represent this pattern. For example, the perpendicular plane cut does not show the highest 3DCS values of the side lobes and the minimum in between is filled by the ridge connecting both lobes. As we will demonstrate below, other cutting planes can be identified showing higher cross-section values for the maxima as well as a greater contrast between the maxima and

the $\phi_2 = 0°$ minimum. Helium, on the other hand, at a first glance shows a completely different behavior. The 3D pattern is dominated by the binary and recoil lobes, and the ridge connecting the two does not appear to be a separate structure originating from a qualitatively different collision sequence. They could arise simply from the geometrical overlap caused by both lobes which are tilted away from the fixed electron's direction due to the postcollision interaction (PCI) between the two emitted electrons. Only the perpendicular plane cut in Fig. 1(f) clearly reveals similar side lobes as observed for $H_2$ but shifted to slightly higher $\phi_2$ values. According to these observations, the higher-order side lobes are present for both targets, but for $H_2$ their visibility is clearer due to a significantly reduced intensity of the binary and recoil lobes.

In the following we discuss the evolution of these higher-order patterns with variation of the fixed electron polar angle $\theta_1$ and of the energy sharing. In Fig. 2 for $H_2$ the part of the experimental 3D 3DCS in the vicinity of the perpendicular plane is magnified for identical energy sharing (4 eV, 12 eV) as before, starting with $\theta_1 = -70°$ via the perpendicular case $\theta_1 = -90°$ to $\theta_1 = -130°$. For quantitative comparison the perpendicular plane cuts are shown in the second column along with He results in the third column. From the 3D images it becomes clear that the strong ridge visible at $\theta_1 = -70°$ shrinks down at $-90°$, showing two small side lobes tilted slightly upward. At $\theta_1 = -130°$ the cross section in the vicinity of the perpendicular plane is almost uniform and the side lobes have essentially disappeared. These observations are quantified in the absolute data shown in the center column. At $\theta_1 = -70°$ the cross-section maxima are almost three times higher than at $-90°$. Then, moving to $-130°$ the magnitude of the peak value is comparable but the pattern has changed to only one maximum for the highest possible relative emission angle of both electrons ($\phi_2 = 0°$). As can be seen in the first column, for increasing $\theta_1$ the recoil peak is strongly affected by the growing postcollision interaction between the two outgoing electrons. Thus, it decreases in magnitude and shifts away from the fixed electron direction until at $\theta_1 = -130°$ the recoil lobe is close to $\theta_2 = 90°$ and contributes significantly to the perpendicular plane cross section. This becomes obvious in particular for the He target with its stronger recoil lobe, where the $\phi_2 = 0°$ maximum monotonically increases from $\theta_1 = -70°$ to $-130°$. For $H_2$ this effect is smaller due to the much reduced recoil lobe size but nevertheless also present.

Finally, in Fig. 3 results for fixed angle $\theta_1 = -90°$ and various energy sharing cases are presented. For symmetric sharing (first row in Fig. 3) the 3D image for $H_2$ shows particularly large side lobes strongly tilted forward and superimposed onto the dominant binary peak. With increasingly asymmetric energy sharing, the side lobes shrink down as visible in Fig. 3(d) for 6 eV, 10 eV followed by Fig. 2(d) for 4 eV, 12 eV and finally dissolve in a uniform filling of the region in between the main binary and recoil lobes for 1 eV, 15 eV [Fig. 3(g)]. In this last case the visible fine structure of the 3D pattern most likely is due to the insufficient statistical significance of the data and results from scattering of the data points, which is visible also in the perpendicular plane cut in Fig. 3(h). The side lobes that dominate the perpendicular plane 3DCS for $H_2$ are hardly visible for He in the 3D pattern [Fig. 2(b)]. Nevertheless, they are present in essentially all perpendicular
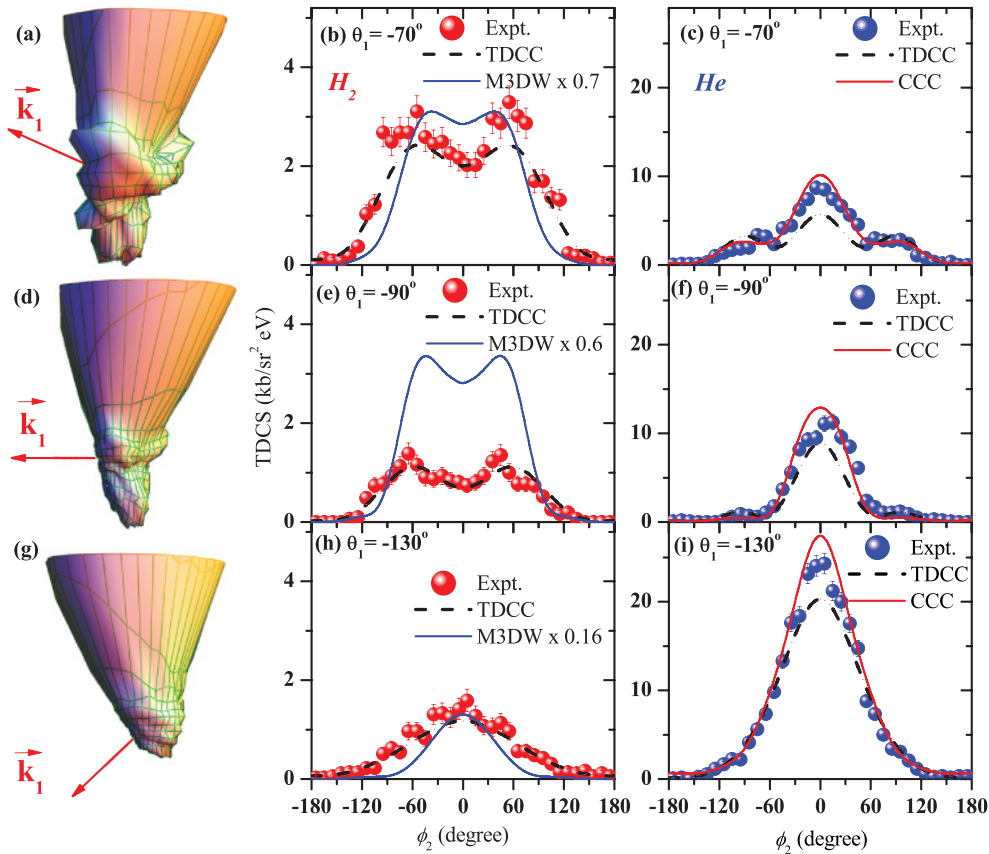
FIG. 2. (Color online) 3DCS for $H_2$ (left and center column) and He (right column) as a function of the emission angle of an electron with $E_2 = 12$ eV. The other electron's ($E_1 = 4$ eV) emission angle $\theta_1$ is fixed: (a) to (c) $\theta_1 = -70°$: (d) to (f) $\theta_1 = -90°$: (e) and (f) $\theta_1 = -130°$. In the left column, excerpts of the 3D-3DCS are given, the center and right columns show cuts along the perpendicular plane.

plane cuts shown for helium in Figs. 2 and 3. They behave according to the corresponding multiple scattering lobes for the $H_2$ case since they are most pronounced for $\theta_1 = -70°$ and asymmetric energy sharing 4 eV, 12 eV, i.e., Figs. 1(f) and 2(b) and, thus, most likely have the same origin.

The perpendicular plane geometry with symmetric sharing 8 eV, 8 eV (Fig. 3, top row) is the particular case discussed by Al-Hagan *et al.* [20] except that their electron energies were slightly higher (10 eV, 10 eV). Consistently with their observation we also find a pronounced double-hump pattern for $H_2$ [Fig. 3(b)], corresponding to a relative angle of both electrons close to 120°. Al-Hagan *et al.* have argued that the pattern for $H_2$ is caused by scattering of the projectile in the atomic potential into the perpendicular plane and subsequent ejection of the target electron. The strongly different pattern for He should result from the same collision sequence but an additional backscattering of one ejected electron in the much deeper ionic potential, with both charges centered at the same point. Our measurements for $H_2$ are consistent with this intuitive picture since back-to-back electron emission becomes more and more important for increasingly asymmetric energy sharing where one electron's energy decreases. Since slow electrons are more susceptible to backscattering in the ionic potential, this case shows the effect of increased backscattering in the ionic potential on the 3DCS cross-section pattern. For He, on the other hand, our systematic measurements

support that the $\phi_2 = 0°$ maximum originates from the binary and recoil lobes, since its height does not show much variation as a function of energy sharing and is always one order of magnitude larger than the higher-order structures in the perpendicular plane discussed for $H_2$. Furthermore, its behavior is not consistent with the side lobes originating from multiple collision sequences. An example can be found in comparing $\theta_1 = -70°$ [Fig. 2(c)] with $-90°$ [Fig. 2(f)]. While the side peaks originating from the double-collision sequence decrease as for the $H_2$ target, the central peak stays constant in height.

In order to highlight similarities and differences in the 3D cross sections for helium and $H_2$, in Fig. 4 an alternative representation of the cross section is given as a 2D color map. Starting from the geometry shown in Fig. 1(a), the detection plane for the electron is rotated around the $y$ axis as illustrated in Fig. 4(a). The cross section is plotted as a function of the emission angle $\phi_2$ within this plane and the detection plane tilting angle $\Theta$. The resulting diagrams for $H_2$ and He in Figs. 4(b) and 4(c), respectively, show the binary lobe at $\Theta \approx 15°$, $\phi_2 = 0°$ and the recoil lobe at $\Theta \approx 170°$, $\phi_2 = 0°$. For He both maxima are interlinked by a ridge along $\phi_2 = 0°$ (dotted line) while for $H_2$ along the $\phi_2 = 0°$ line there are two minima at $\Theta = 120°$ and $\Theta = 60°$. The multiple scattering lobes discussed above are visible for both target species as two ridges marked by dashed lines left and right from the center $\phi_2 = 0°$ and
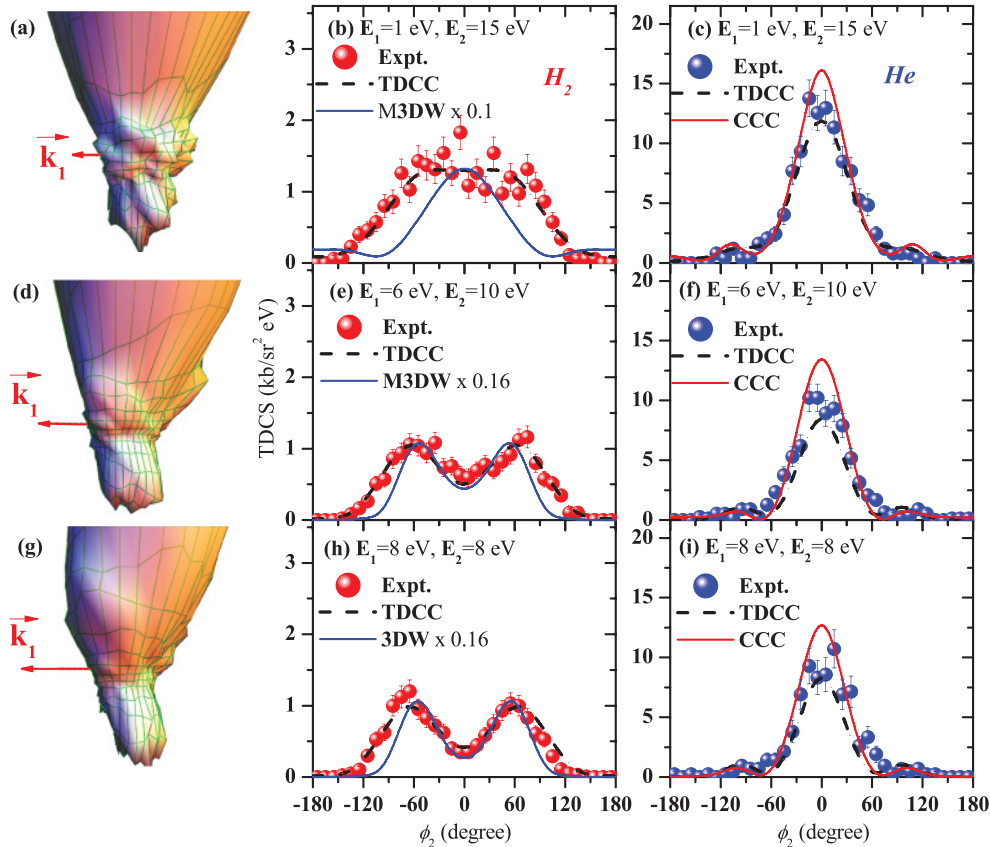
FIG. 3. (Color online) 3DCS for $H_2$ (left and center column) and He (right column) as a function of the emission angle of one electron with the other electron's emission angle fixed to $\theta_1 = -90°$. From top to bottom row the energy sharing is: (a) to (c) $E_1 = 8$, $E_2 = 8$ eV: (d) to (f) $E_1 = 6$, $E_2 = 10$ eV: (g) and (i) $E_1 = 1$, $E_2 = 15$ eV. In the left column, excerpts of the 3D-3DCS are given. The center and right columns show cuts along the perpendicular plane, i.e. both electrons are emitted in the perpendicular plane.

extended over the full $\Theta$ range. They emerge from the binary lobe for small $\Theta$ and again are linked to the binary lobe for large $\Theta$. Cross-section cuts for the particular $\Theta$ angles 60°, 90°, and 120° are shown in the right column of Fig. 4. It is obvious that the double-lobe pattern shows a deeper central minimum for $\Theta$ angles of 120° and 60° compared to the 90° case since the perpendicular plane is close to the cross-section ridge, which peaks around $\Theta \approx 85°$. For helium at 120° the side peaks are more separated from the dominant central peak.

### A. Comparison with theory

Discussing first the $H_2$ results, the M3DW model reproduces the cross-section shapes in both the coplanar as well as the perpendicular geometries shown. Thus, the underlying interactions and mechanisms responsible for the structure of the 3DCS are well included. Deviations are an overestimation of the recoil peak in Fig. 1(c) and for all perpendicular plane data the peak widths are too small, indicating some deficiencies in the momentum profile of the bound target electron wave function. Finally, the absolute cross-section magnitudes are overestimated considerably, as can be seen by the correction factors given in the legends of the figures. For Figs. 1 and 2 these correction factors are determined for optimal agreement with experiment of the binary peak magnitude in the scattering

plane, as can be seen in Fig. 1(c). In most cases this results also in good agreement of the perpendicular plane cross section except for $E_1 = 4$ eV, $E_2 = 12$ eV, and $\theta_1 = -90°$ [Fig. 2(e)]. For Fig. 3 M3DW results for the perpendicular plane only are available and therefore the scaling factors were obtained for best fit in the perpendicular plane [Figs. 3(b), 3(e), and 3(h)].

The nonperturbative TDCC results are in very good agreement concerning shape and absolute cross-section magnitude for all perpendicular plane results shown here. Surprisingly, the only deviations concern the first-order structures in the scattering plane shown in Fig. 1(c). The binary peak is slightly too high and shifted to slightly larger angles. Furthermore, the recoil peak is strongly underestimated and barely visible. A global 3D view of the TDCC results is shown in Fig. 5 for two exemplary kinematical cases. In Fig. 5(a) the TDCC results corresponding to the experimental data in Fig. 1(a) are presented ($E_1 = 4$ eV, $E_2 = 12$ eV, $\theta_1 = -70°$). The higher-order ridge in the vicinity of the perpendicular plane is nicely reproduced except that the experimental pattern appears to have more pronounced side peaks. The same is true when comparing the symmetric energy sharing case in Fig. 5(b) ($E_1 = E_2 = 8$ eV, $\theta_1 = -90°$) with experiment in Fig. 3(a). The forward-tilted side lobe is not visible in the calculation. In addition, in both cases the theory underestimates the recoil lobe size, as mentioned above.
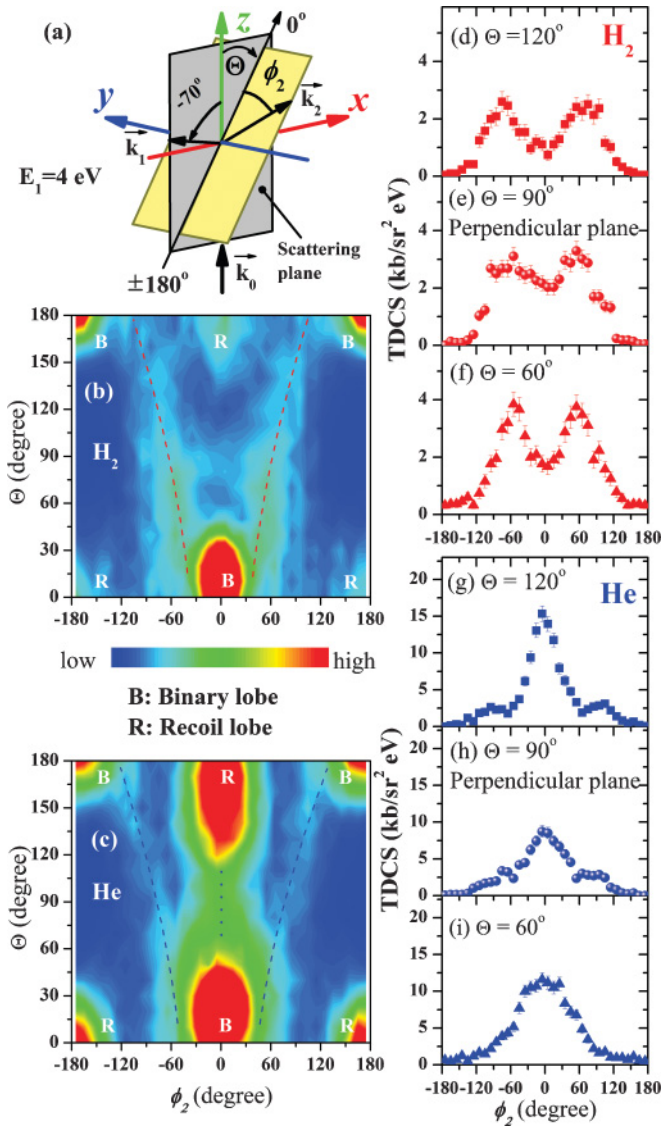
FIG. 4. (Color online) (a) Geometry of the $(e, 2e)$ kinematics with $\vec{k}_1$ ($E_1 = 4$ eV) fixed to $\theta_1 = -70°$. The second electron emission of $\vec{k}_2$ ($E_2 = 12$ eV) is plotted as a function of $\phi_2$ angle in a plane, which is perpendicular to the scattering plane and rotated by the angle of $\Theta$ around the $y$-axis: (b) and (c) the resulting cross section diagrams for $H_2$ and He plotted as a two-dimensional color map as function of angles $\Theta$ and $\phi_2$: (d)–(f) the cross sections of $H_2$ plotted as a function of $\phi_2$ for different $\Theta$ angles indicated in the diagrams and as horizontal dotted lines in (b): (g)–(i) same as (d)–(f) but for He.



FIG. 5. (Color online) TDCC results for the 3DCS of the $H_2$ target covering $4\pi$ solid angle of electron emission. (a) $E_1 = 4$ eV, $E_2 = 12$ eV, $\theta_1 = -70°$. (b) $E_1 = E_2 = 8$ eV, $\theta_1 = -90°$.

TDCC curve would result in slightly too high side maxima of the theory.

## V. CONCLUSION

We have presented a comprehensive experimental and theoretical study of low-energy electron-impact ionization for $H_2$ and He targets. Observing the full solid angle of one emitted electron, we demonstrate that the perpendicular plane structures assigned to multiple projectile scattering processes by Al-Hagan *et al.* [20] originates from two side lobes tilted out of the scattering plane. The size and shape of these lobes sensitively depend on the details of the collision kinematics, as was shown by varying the emission angle of the second electron out of the perpendicular plane and the energy sharing among both final state electrons. The absolute normalization of the data allowed a quantitative comparison of the cross-section magnitude at the various geometries and for both target species. It turns out that the side lobes can be enhanced significantly compared to the frequently studied perpendicular geometry if one electron's polar angle $\theta_1$ is changed from 90° to 70°. In addition, the strong maximum observed for He for back-to back emission of both electrons is mainly due to the overlapping of the binary and recoil lobes in this region. There are two underlying differences between the $H_2$ and He targets: First, the much wider Compton profile of He enhances the first-order binary and recoil lobes compared to the higher-order structures. Second, the relative magnitude of the recoil lobe for He is higher and shifted in angle away from the fixed electron. In order to highlight the common multiple scattering patterns for $H_2$ and He, we have introduced a different representation of the 3D 3DCS. As a result, particular cuts in the 3D pattern can be found where the side maxima are particularly strong and more separated from the first-order lobes.

Finally, our absolutely normalized cross sections provide a benchmark test for theory, revealing discrepancies not only in shape but also in absolute magnitude. Here the nonperturbative TDCC and CCC models in general are in good agreement with experiment. For He a few remaining small discrepancies are found for the TDCC model in situations where higher-order contributions are large. For $H_2$ the most severe discrepancy is a strong underestimation of the recoil lobe. The perturbative M3DW model shows

Coming now to the helium target, we see good agreement in shape and magnitude for both the TDCC and also the CCC calculations. Remaining discrepancies can be found in the perpendicular plane for the $\phi_2 = 0°$ maximum where the CCC result is always higher than the TDCC. The peak ratio can be as high as 2.0 in Fig. 1(f) although for other cases this difference is much smaller. Both models also differ in the size of the side maxima. Given the experimental uncertainties concerning the absolute scaling of the cross section, Fig. 1(f) indicates that the CCC result is in slightly better agreement since a scaling of the experimental results to fit the $\phi_2 = 0°$ maximum of the
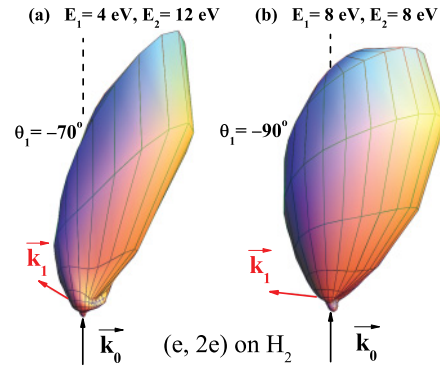
discrepancies concerning the absolute magnitude up to a factor of 6. The cross-section shapes are qualitatively reproduced with some deviations in the widths of the cross-section maxima.

Finally, it turns out that the chosen energy regime is particularly suited to the study of multiple collision reactions and is a compromise between higher impact energies, where the contribution of multiple collisions goes down, and lower energies, where the observed emission pattern is dominated by PCI as was demonstrated previously [22]. In addition, ionization of bound orbitals with a low momentum spread is advantageous, suppressing first-order ionization processes and to avoid a strong broadening and merging of the resulting cross-section structures. This can be realized in the present projectile energy regime for ionizing, e.g., the valence orbitals of ground state or excited alkali-metal atoms.

[1] T. N. Resigno *et al.*, Science **286**, 2474 (1999).

[2] I. Bray, Phys. Rev. Lett. **89**, 273201 (2002).

[3] J. Colgan and M. S. Pindzola, Phys. Rev. A **74**, 012713 (2006).

[4] J. Colgan *et al.*, J. Phys. B **42**, 145002 (2009).

[5] A. S. Kheifets, D. V. Fursa, C. W. Hines, I. Bray, J. Colgan, and M. S. Pindzola, Phys. Rev. A **81**, 023418 (2010).

[6] J. Colgan, M. S. Pindzola, F. Robicheaux, C. Kaiser, A. J. Murray, and D. H. Madison, Phys. Rev. Lett. **101**, 233201 (2008).

[7] Ren *et al.*, J. Phys. B **43**, 035202 (2010).

[8] D. H. Madison and O. Al-Hagan, J. At. Mol. Opt. Phys. **2010**, 1 (2010).

[9] A. J. Murray *et al.*, J. Phys. B **25**, 3021 (1992).

[10] X. Zhang *et al.*, J. Phys. B **23**, L173 (1990).

[11] M. Schulz *et al.*, Nature (London) **422**, 48 (2003).

[12] M. Durr, C. Dimopoulou, B. Najjari, A. Dorn, K. Bartschat, I. Bray, D. V. Fursa, Z. Chen, D. H. Madison, and J. Ullrich, Phys. Rev. A **77**, 032717 (2008).

[13] M. Durr, C. Dimopoulou, B. Najjari, A. Dorn, and J. Ullrich, Phys. Rev. Lett. **96**, 243202 (2006).

[14] A. J. Murray and F. H. Read, Phys. Rev. A **47**, 3724 (1993).

[15] M. Schulz, M. Dürr, B. Najjari, R. Moshammer, and J. Ullrich, Phys. Rev. A **76**, 032712 (2007).

[16] M. Foster, J. L. Peacher, M. Schulz, D. H. Madison, Z. Chen, and H. R. J. Walters, Phys. Rev. Lett. **97**, 093202 (2006).

[17] D. S. Milne-Brownlie, M. Foster, J. Gao, B. Lohmann, and D. H. Madison, Phys. Rev. Lett. **96**, 233201 (2006).

[18] E. M. Staicu Cassagrande *et al.*, J. Phys. B **41**, 025204 (2008).

[19] S. Chatterjee, D. Misra, A. H. Kelkar, L. C. Tribedi, C. R. Stia, O. A. Fojon, and R. D. Rivarola, Phys. Rev. A **78**, 052701 (2008).

[20] Al-Hagan *et al.*, Nature Phys. **5**, 59 (2009).

[21] J. Colgan, O. Al-Hagan, D. H. Madison, C. Kaiser, A. J. Murray, and M. S. Pindzola, Phys. Rev. A **79**, 052704 (2009).

[22] O. Al-Hagan, A. J. Murray, C. Kaiser, J. Colgan, and D. H. Madison, Phys. Rev. A **81**, 030701 (2010).

[23] K. L. Nixon, A. J. Murray, and Ch. Kaiser, J. Phys. B **43**, 085202 (2010).

[24] M. Takahashi, N. Watanabe, Y. Khajuria, Y. Udagawa, and J. H. D. Eland, Phys. Rev. Lett. **94**, 213202 (2005).

[25] S. Bellm, J. Lower, E. Weigold, and D. W. Mueller, Phys. Rev. Lett. **104**, 023202 (2010).

[26] A. Senftleben *et al.*, J. Phys. B **43**, 081002 (2010).

[27] J. Ullrich *et al.*, Rep. Prog. Phys. **66**, 1463 (2003).

[28] M. Dürr *et al.*, J. Phys. B **39**, 4097 (2006).

[29] J. Röder *et al.*, J. Phys. B **29**, 2103 (1996).

[30] X. Ren *et al.*, J. Phys.: Conf. Ser. **212**, 012003 (2010).

[31] T. Rösel *et al.*, J. Phys. B **25**, 3859 (1992).

[32] T. W. Shyn, W. E. Sharp, and Y. K. Kim, Phys. Rev. A **24**, 79 (1981).

[33] J.-S. Yoon *et al.*, J. Phys. Chem. Ref. Data **37**, 913 (2008).

[34] M. S. Pindzola *et al.*, J. Phys. B **40**, R39 (2007).

[35] J. Colgan, O. Al-Hagan, D. H. Madison, C. Kaiser, A. J. Murray, and M. S. Pindzola, Phys. Rev. A **79**, 052704 (2009).

[36] J. Colgan *et al.*, J. Phys. B **42**, 145002 (2009).

[37] J. Gao, J. L. Peacher, and D. H. Madison, J. Chem. Phys. **123**, 204302 (2005).

[38] J. Gao, D. H. Madison, and J. L. Peacher, J. Chem. Phys. **123**, 204314 (2005).

[39] I. Bray and D. V. Fursa, Phys. Rev. A **54**, 2991 (1996).

[40] A. T. Stelbovics, I. Bray, D. V. Fursa, and K. Bartschat, Phys. Rev. A **71**, 052716 (2005).

[41] I. Bray, T. Lepage, D. V. Fursa, and A. T. Stelbovics, J. Phys. B **43**, 074028 (2010).

[42] I. Bray, D. V. Fursa, A. S. Kadydov, and A. T. Stelbovics, Phys. Rev. A **71**, 052716 (2005).

[43] Y.-K. Kim *et al.*, NIST Standard Reference Database **107** (2005).